



Influence of temperature and strain rate on hot deformation behavior of $Zr_{50}Ti_{50}$ alloy in single β field

Yun-kai ZHOU¹, Zhi-hao FENG¹, Chao-qun XIA¹, Wen-chang LIU¹, Qin JING¹,
Shun-xing LIANG², Ming-zhen MA¹, Zhi-guo ZHANG¹, Xin-yu ZHANG¹, Ri-ping LIU¹

1. State Key Laboratory of Metastable Materials Science and Technology,
Yanshan University, Qinhuangdao 066004, China;

2. College of Equipment Manufacture, Hebei University of Engineering, Handan 056038, China

Received 29 July 2015; accepted 31 October 2015

Abstract: The deformation behavior and microstructure of the $Zr_{50}Ti_{50}$ alloy in β phase field were investigated by isothermal compression tests at temperatures ranging from 700 to 850 °C and strain rates ranging from 0.001 to 1 s⁻¹. The flow curves exhibited typical flow softening. The initial discontinuous yielding behavior was observed at higher strain rates, which was not found in other traditional Zr alloys. The apparent deformation activation energy was calculated to be 103 kJ/mol and constitutive equation describing the flow stress as a function of the strain rate and deformation temperature was proposed. The analysis indicated that the hot deformation mechanism was mainly dominated by dynamic recovery. However, dynamic recrystallization was delayed by dynamic recovery. Thereafter, the processing map was calculated to evaluate the efficiency of the forging process at the temperatures and strain rates investigated and to optimize processing parameters of hot deformation. The optimum processing parameters were found to be 830–850 °C and 0.56–1 s⁻¹ for hot the deformation of $Zr_{50}Ti_{50}$ alloy in the β phase region.

Key words: Zr alloy; hot deformation; apparent activation energy; microstructure; processing map

1 Introduction

Zr alloys are widely used in the nuclear and chemical industries because of their superior properties, such as small thermal neutron absorption, low thermal expansion coefficient [1], good corrosion resistance [2,3] and excellent compatibility with fuel and coolant [4,5]. However, traditional Zr alloys with relatively low strength does not meet the high strength requirement as structural materials. Thus, new Zr alloys with high strength and good ductility are manufactured [6–10]. Moreover, $Zr_{50}Ti_{50}$ alloy has shown good mechanical properties among the new Zr alloys manufactured [7,8].

Hot working is very important in metallic material fabrication processes since this step is used to obtain desired microstructure and mechanical properties. However, extensive researches on hot deformation behavior of traditional Zr alloys were carried out and optimum hot working conditions were determined so

far [11–16]. CHAKRAVARTTY et al [11,12] found that dynamic recrystallization occurred in commercially pure Zr where deformation was performed in the temperature range of 730–850 °C at strain rates of 0.01 to 1 s⁻¹. However, Zr–1Nb–1Sn alloy displayed dynamic recovery in α field, dynamic recrystallization in $\alpha+\beta$ field and superplasticity in β field during hot deformation [15]. Contradictorily, it was mentioned in Ref. [16] that dynamic recovery occurred in β field in the case of Zr–1Nb alloy.

In order to understand the hot deformation behavior clearly and to optimize the processing parameters of forged $Zr_{50}Ti_{50}$ binary alloy, in this study, hot deformation behavior and microstructure evolution after isothermal compression in β phase field of $Zr_{50}Ti_{50}$ binary alloy were investigated. The variation of flow stress with processing conditions (deformation temperature and strain rate) was subsequently analyzed. Furthermore, the apparent deformation activation energy was calculated from the flow stress. And the apparent

deformation activation energy and flow stress are key parameters to characterize the hot deformation behavior [17,18].

And the processing map based on dynamic materials model has been developed to optimize processing parameters and to understand the metals hot deformation [19–22]. So, the processing map was also used to analyze the hot deformation behavior of isothermally compressed $Zr_{50}Ti_{50}$ binary alloy. The results may help to optimize the processing conditions of forging of $Zr_{50}Ti_{50}$ binary alloy.

2 Experimental

Sponge Zr ($w(Zr+Hf) \geq 99.5\%$) and sponge Ti (99.7%, mass fraction) were used to prepare the $Zr_{50}Ti_{50}$ (mole fraction, %) alloy. The alloy ingots were melted four times using a vacuum induction melting furnace to ensure uniform chemical composition. The cast ingot was breakdown into rods of 40 mm in diameter. In order to eliminate the effect of initial microstructures, the rods were heat-treated at 1050 °C for 4 h in a tubular vacuum furnace with protective argon atmosphere followed by furnace cooling.

Cylindrical specimens of 6 mm in diameter and 9 mm in height were machined from these rods. The $\alpha \rightarrow \beta$ phase transformation temperature (β transus temperature) of this material was determined by phase diagram and differential scanning calorimeter. The β transus temperature was determined to be about 600 °C. Hot compression tests were conducted using a Gleeble-3500 thermo-mechanical simulator at temperatures of 700–850 °C and at strain rates of 0.001–1 s⁻¹. In the Gleeble, specimens were heated through the direct resistance heating system. The temperature was controlled within ± 3 °C using Pt–Rh–Pt thermocouple which was spot-welded at the mid-span of the specimens. The graphite lubricant and tantalum foils were used to reduce the friction between the cylindrical specimens and anvil. The specimens were heated to the test temperature (700–850 °C) at a rate of 20 °C/s in an argon atmosphere, held for 10 min. Each of the specimen was thereafter compressed to a true strain of 0.7 at strain rates of 0.001–1 s⁻¹. Subsequently, the specimens were water-quenched.

The deformed specimens were sectioned along the compression axis through the center. Samples for optical microscopy were prepared using standard metallographic techniques. Thereafter, the polished surfaces were chemically etched using a solution of 15% hydrofluoric acid (HF), 5% nitric acid (HNO₃) and 80% distilled water (H₂O).

3 Results and discussion

3.1 Stress–strain curves

The stress–strain curves obtained from the compression tests are presented in Fig. 1. The curves show flow softening in which the flow stress reaches a peak value at a certain strain and then decreases to a steady state with increasing the strain. In addition, the degree of flow softening decreases with increasing the deformation temperature. The mechanisms of softening are balance of the rate of work hardening, e.g., dynamic recrystallization, superplasticity or dynamic recovery [23].

Initial discontinuous drop in the flow stress upon yielding followed by a gradual change in the plastic flow behavior is observed with increasing strain. This behavior is different from those of Zr and traditional Zr alloys [11–16]. However, the discontinuous yielding phenomenon is not observed at the lowest strain rate of 0.001 s⁻¹. The discontinuous yielding has been found in Ti alloys deformed in β phase field [24–28]. This indicates that the hot deformation behavior of Zr alloys may be changed with Ti addition. The dependency of yield drop in flow stress on strain rate and temperature is shown in Fig. 2. It is observed that the magnitude of yield drop decreased with increasing the deformation temperature and oppositely with decreasing the strain rate. This is in agreement with the results reported by SRINIVASAN [25] and PHILIPPART and RACK [29]. During initial deformation process, dislocations rapidly multiply and block at grain boundary, resulting in the increase of flow stress. Then, the dislocation may break down and the grain boundary acts as the sources of mobile dislocations with increasing strain. Thus, increased mobile dislocation density can reduce flow stress value. So, the discontinuous yield drop should be due to the origin of mobile dislocations being grain boundary dislocation sources, which was reported by PHILIPPART and RACK [29]. With increasing deformation temperature and decreasing strain rate, the discontinuous yielding can be eliminated through thermally-assisted dislocations motion and reducing the work-hardening levels, respectively [25,29]. As a result, the magnitude of the discontinuous yield drop decreased with increasing deformation temperature and decreasing strain rate.

However, it is difficult to discuss the hot deformation behavior using only stress–strain curves. Hence, detail investigation will be discussed in the following sections using the kinetic analysis, microstructure and processing map.

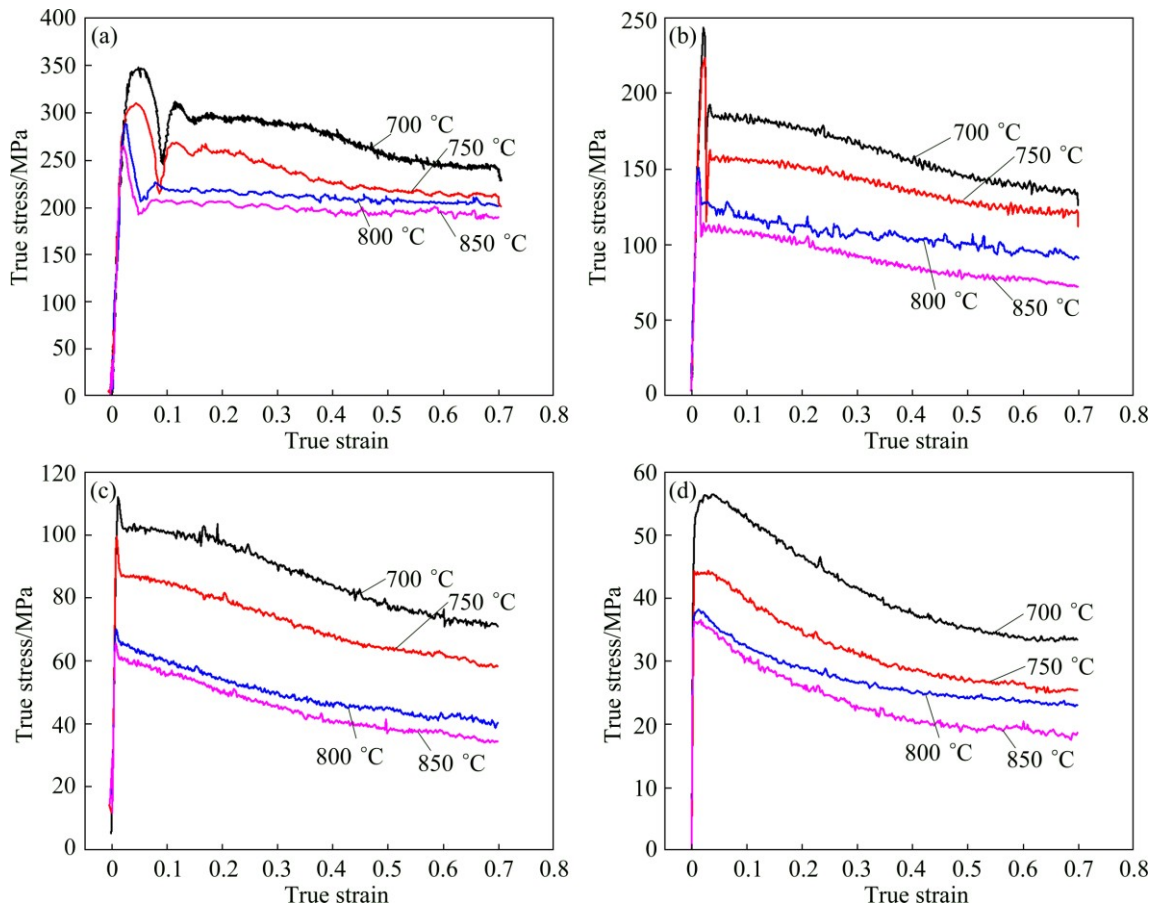


Fig. 1 Stress–strain curves of $Zr_{50}Ti_{50}$ alloy deformed at different strain rates: (a) 1 s^{-1} ; (b) 0.1 s^{-1} ; (c) 0.01 s^{-1} ; (d) 0.001 s^{-1}

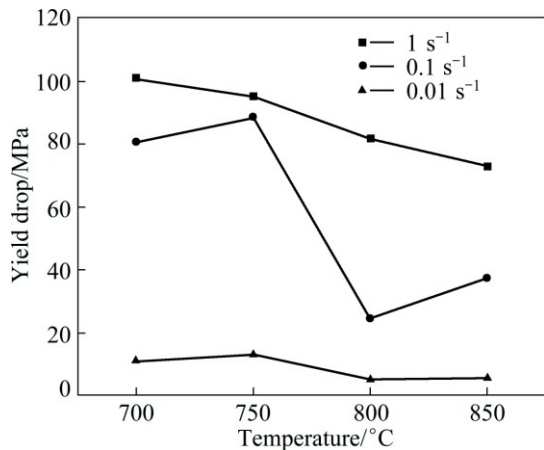


Fig. 2 Magnitude of yield drop of $Zr_{50}Ti_{50}$ alloy as function of temperature and strain rate

3.2 Kinetic analysis

The stress–strain curves reveal that the flow stress is strongly affected by strain rate and deformation temperature. The peak stress, i.e., the highest flow stress in the flow curves, usually can be chosen as the representative stress of each flow curve. Constitutive equation is constructed to understand the hot deformation behavior of $Zr_{50}Ti_{50}$ alloy. In addition, the apparent deformation activation energy is also calculated.

The temperature and strain rate dependence of flow stress in hot deformation is generally expressed by the Arrhenius-type equation [30–32]:

$$\dot{\epsilon} = A[\sinh(\alpha\sigma_p)]^n \exp[-Q/(RT)] \quad (1)$$

where $\dot{\epsilon}$ is the strain rate (s^{-1}), A and α are material constants, n is the stress exponent, σ_p is the peak stress (MPa), Q is the apparent deformation activation energy (J/mol), R is the molar gas constant, and T is the deformation temperature (K).

From Eq. (1), we can express

$$Q = Rn \left\{ \frac{\partial \ln[\sinh(\alpha\sigma_p)]}{\partial (1/T)} \right\}_{\dot{\epsilon}} \quad (2)$$

The plot of $\ln \dot{\epsilon}$ versus $\ln[\sinh(\alpha\sigma_p)]$ and the plot of $\ln[\sinh(\alpha\sigma_p)]$ versus $1000/T$ in the β phase region (700–850 °C) are shown in Figs. 3(a) and (b), respectively. The apparent deformation activation energy is derived from the peak stress. From Eq. (1), the value of n is calculated using the average slope value of $\ln \dot{\epsilon} - \ln[\sinh(\alpha\sigma_p)]$. The value of s (average slope value of $\ln[\sinh(\alpha\sigma_p)] - 1000/T$) is also calculated. Then, the mean values of the slopes (n and s) are used to calculate the activation energy, $Q = R \cdot n \cdot s = 103274\text{ J/mol}$. This value is consistent with the values reported in the literatures for

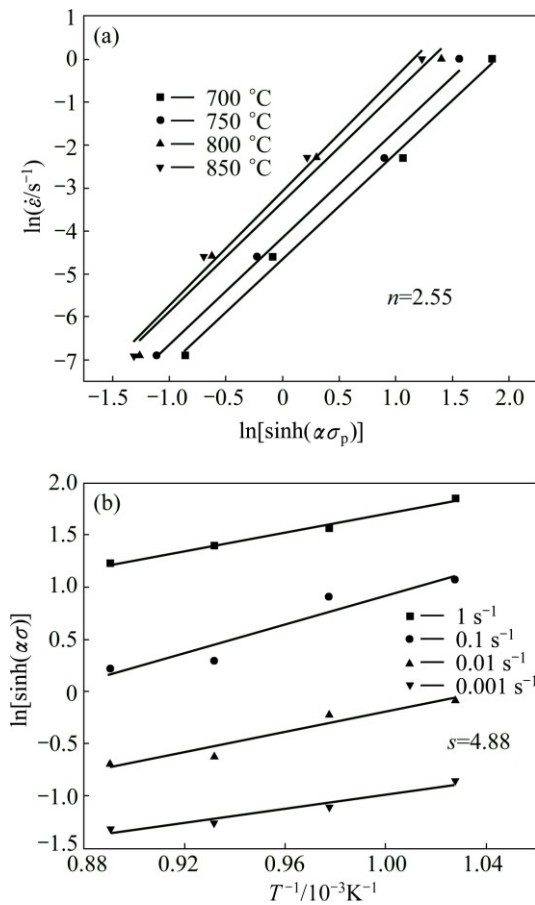


Fig. 3 Plot of $\ln \dot{\epsilon}$ vs $\ln[\sinh(\alpha\sigma_p)]$ (a) and plot of $\ln[\sinh(\alpha\sigma_p)]$ vs $1000/T$ (b)

other Zr alloys. For instance, the value of deformation activation energy in the β phase region is found to be 110 kJ/mol for Zr [33], 110 kJ/mol for Zr–1Nb–1Sn alloy [15] and 120 kJ/mol for Zr–2.5Nb alloy [14]. The activation energy value obtained in the present study is close to the value of self-diffusion activation energy of β -Zr (110 kJ/mol) [14]. CHARKRAVARTTY et al [15] reported that hot deformation associated accommodation mechanism of Zr alloys in the single β field is controlled by self-diffusion when the value of activation energy is close to that of self-diffusion of β -Zr. Thus, the mechanism of hot deformation of $Zr_{50}Ti_{50}$ alloy would be the dynamic recovery. Furthermore, the value of stress exponent (n) is found to be 2.55 (between 2 and 3, see Fig. 3(a)) which suggests that the underlying rate-controlling accommodation mechanism is grain boundary sliding [34].

Figure 4 shows the strain rate temperature parameter Z (called Zener–Hollomon) with a correlation coefficient of 0.994. It is evident that the peak stress increased with increasing Z parameter. And the linear relationship between parameter Z and peak stress indicates the Arrhenius-type equation is appropriate to describe the dependence of the peak stress on

deformation temperature and strain rate. Based on the experimental results, the constitutive equation (Eq. (1)) for isothermal hot working of $Zr_{50}Ti_{50}$ alloy in the β field can be written as

$$\dot{\epsilon} = 3162.13[\sinh(0.00732\sigma_p)]^{2.55} \exp[-103274/(RT)] \quad (3)$$

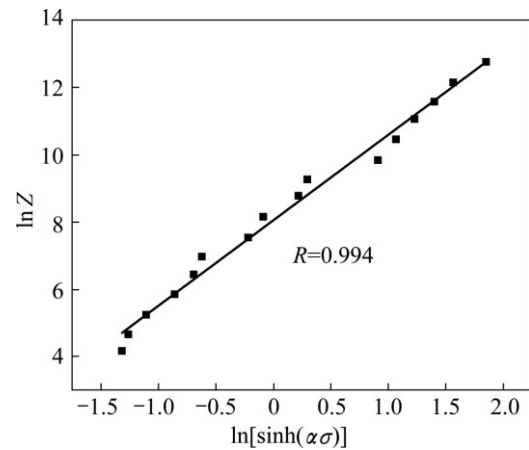


Fig. 4 Relationship between peak stress (σ_p) and Zener–Hollomon (Z) parameter of $Zr_{50}Ti_{50}$ alloy

3.3 Deformed microstructure

Figure 5 shows typical microstructures of $Zr_{50}Ti_{50}$ alloy after hot deformation at different temperatures and strain rates. Elongated β grains along the radial direction are observed after the sample deformed at temperature of 700 °C with strain rate of 1 s⁻¹ (Fig. 5(a)). The flow localization is also observed in the sample. However, with increasing the deformation temperature, a few recrystallized grains along the grain boundaries are found (Fig. 5(c)). In addition to a few recrystallized grains, there are some serrated grain boundaries at the temperatures of 700 and 850 °C and a lower strain rate of 0.001 s⁻¹ (Figs. 5(b) and (d)).

From the kinetic analysis, the hot deformation associated accommodation mechanism of $Zr_{50}Ti_{50}$ alloy is strongly controlled by self-diffusion. As a result, self-diffusion may promote the dynamic recovery process and delay the dynamic recrystallization process [35]. Moreover, due to the strong effect of dynamic recovery in the sample deformed at higher temperature or lower strain rate, only a few recrystallized grains are visible along the grain boundaries as enough driven force for recrystallization nucleation was not found. So, in the present study, microstructural observation indicates that hot deformation mechanism is mainly dominated by dynamic recovery, whereas dynamic recrystallization is delayed.

The serrated grain boundaries are probably caused by the grain boundaries migration. During hot deformation, dislocations may glide through grain boundary and leave behind the gliding step, which will

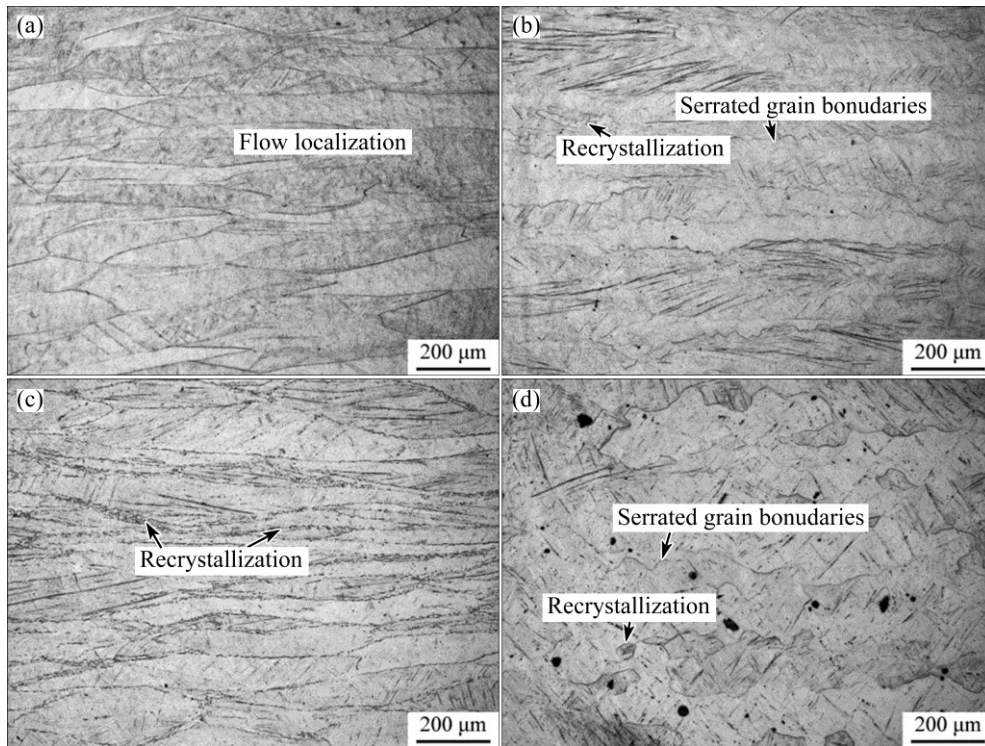


Fig. 5 Optical microstructures of $Zr_{50}Ti_{50}$ alloy under different deformation conditions: (a) 700 °C, 1 s⁻¹; (b) 700 °C, 0.001 s⁻¹; (c) 850 °C, 1 s⁻¹; (d) 850 °C, 0.001 s⁻¹

lead to grain boundaries migration. The grain boundaries migration ultimately changes the smooth grain boundaries into serration.

3.4 Construction of processing map

The processing map is very useful to optimize processing parameters and to control microstructure [23]. The processing maps with different strains are usually constructed on the basis of the principles of dynamic materials model for the optimum hot working condition [36]. According to the dynamic materials principles, hot working process can be regarded as a closed system, where the total power (p) absorbed in the hot working process is dissipated through the temperature rise and microstructure evolution of the work-piece [37]. The named G content and J co-content are used to represent the dissipation powers caused by the temperature rise and microstructure evolution, respectively. The partition of the total input power between G and J depends on the strain rate sensitivity of flow stress (m). For an ideal linear dissipater ($m=1$), the maximum value of J is supposed to be $p/2$. This will result in a dimensionless parameter called efficiency of power dissipation (η) of a non-linear dissipater and expressed as [37]:

$$\eta = \frac{J}{J_{\max}} = \frac{2m}{m+1} \quad (4)$$

The power dissipation map is constructed using the

variation of η with temperature and strain rate, which may directly show the optimum processing parameters for hot working. A continuum instability criterion is developed based on the extreme principle of irreversible thermodynamics to identify the regime of flow instability, as given in Ref. [23]:

$$\xi(\dot{\epsilon}) = \frac{\partial \lg[m/(m+1)]}{\partial \lg \dot{\epsilon}} + m < 0 \quad (5)$$

where $\dot{\epsilon}$ is the strain rate and $\xi(\dot{\epsilon})$ is a dimensionless instability parameter. An instability map is constituted using the variation of $\xi(\dot{\epsilon})$ with respect to temperature and strain rate. The flow instability is predicted when $\xi(\dot{\epsilon})$ is negative [38,39]. In addition, the instability map is superimposed on a power dissipation map to construct a processing map.

For the $Zr_{50}Ti_{50}$ alloy, the processing map with different strains is shown in Fig. 6. The shaded areas indicate the flow instability regions and the contour number represents the efficiency of power dissipation. With increasing strain, initially the instability region extended to lower strain rate and higher temperature and then gradually decreased. It is clear that there are two domains with the peak efficiency of power dissipation, one domain (called Domain A) at the temperatures from 730 to 755 °C with strain rates varying from 0.0018 to 0.001 s⁻¹, the other domain (called Domain B) in the temperature range from 830 to 850 °C and strain rate range from 0.56 to 1 s⁻¹. The peak efficiencies of power

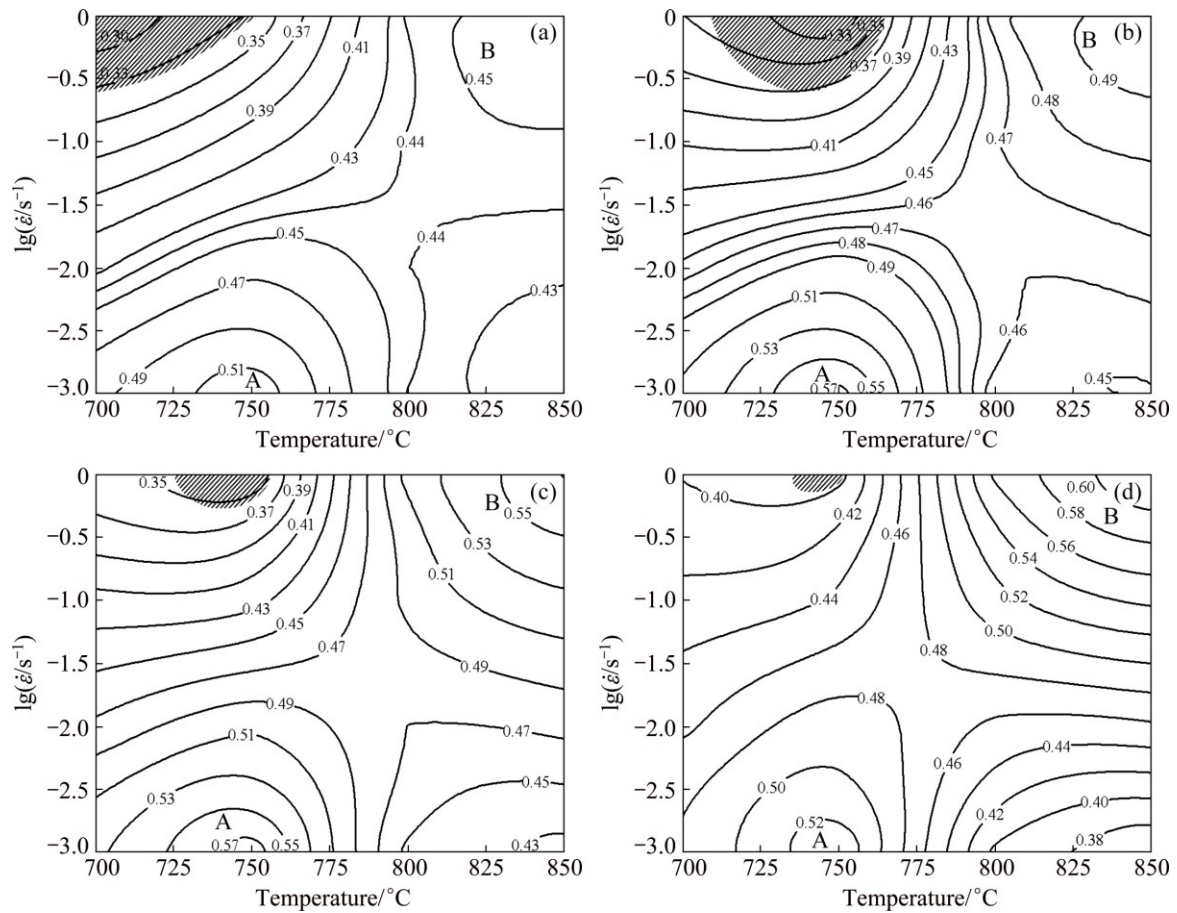


Fig. 6 Processing maps of $Zr_{50}Ti_{50}$ alloy at true strains of 0.1 (a), 0.3 (b), 0.5 (c) and 0.7 (d)

dissipation in the aforementioned domains were found to be 0.54 and 0.62 at the strain of 0.7, respectively.

Figure 7 shows the variation in the peak efficiency of power dissipation with true strain at the two domains for the $Zr_{50}Ti_{50}$ alloy. In Domain A, it is clear that the efficiency of power dissipation increased slightly to the peak value, then decreased with increasing strain at the temperature of 750 °C and strain rate of 0.001 s^{-1} . In

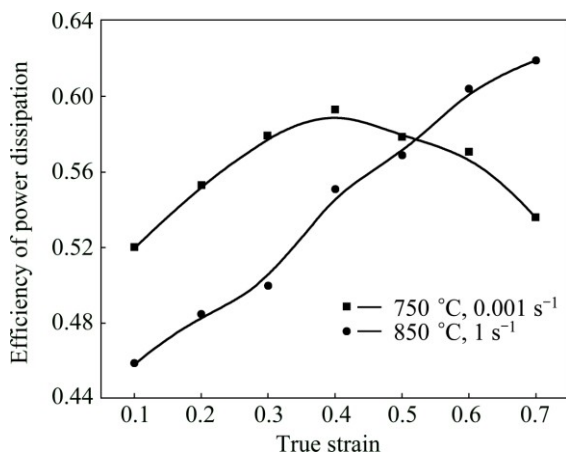


Fig. 7 Variation in efficiency of power dissipation with true strain under deformation conditions of 750 °C, 0.001 s^{-1} and 850 °C, 1 s^{-1}

Domain B, the efficiency of power dissipation increased with increasing strain at the temperature of 850 °C and strain rate of 1 s^{-1} . Moreover, the efficiency of power dissipation was more than 0.6 at large strain in Domain B. Similar results were reported by CHAKRAVARTTY et al [33] which may represent the super plasticity in β field. Thus, Domain B may be considered to be an optimum hot working condition in the case of large deformation. The typical microstructure of Domain B is shown in Fig. 5(c) with recrystallized grains along the grain boundaries.

4 Conclusions

1) The flow curves showed significant flow softening with a peak stress. Unlikely to other Zr alloys, a significant initial discontinuous yielding is found in the $Zr_{50}Ti_{50}$ alloy flow curves at low temperatures and high strain rates. The yield drop decreases with increasing deformation temperature and decreasing strain rate.

2) The peak stress decreases with increasing deformation temperature and decreasing strain rate. The dependence of the peak stress on deformation temperature and strain rate can be described by an

empirical Arrhenius-type equation:

$$\dot{\epsilon} = 3162.13[\sinh(0.00732\sigma_p)]^{2.55} \exp[-103274/(RT)].$$

3) The deformation activation energy is calculated to be 103 kJ/mol, which is close to the self-diffusion activation energy of β -Zr. Hence, it is assumed that dynamic recovery becomes dominant deformation mechanism of Zr₅₀Ti₅₀ alloy. In addition, the microstructural observation confirms that dynamic recrystallization is delayed due to the dynamic recovery.

4) According to the processing map, for the Zr₅₀Ti₅₀ alloy, the optimum processing parameters for hot working are found to be 830–850 °C and 0.56–1 s⁻¹.

References

- [1] FRANKLIN D G, LUCAS G E, BEMENT A L. Creep of zirconium alloy in nuclear reactors [M]. Philadelphia: ASTM STP 815, 1983: 183–201.
- [2] JUNG Y, SEOL Y N, CHOI B K, PARK J Y. Behavior of stress–relaxation and the estimation of creep in Zr–1.1Nb–0.05Cu alloy [J]. Mater Des, 2012, 42: 118–123.
- [3] NEOGY S, SRIVASTAVA D, CHAKRAVARTTY J K, DEY G K. Microstructural evolution in Zr–1Nb and Zr–1Nb–1Sn–0.1Fe alloys [J]. Metal Trans A, 2007, 38: 485–498.
- [4] ZHOU F Y, WANG B L, QIU K J, LIN W J, LI L, WANG Y B, NIE F L, ZHENG Y F. Microstructure, corrosion behavior and cytotoxicity of Zr–Nb alloys for biomedical application [J]. Mater Sci Eng C, 2012, 32: 851–857.
- [5] LIANG S X, MA M Z, JING R, ZHOU Y K, JING Q, LIU R P. Preparation of the ZrTiAlV alloy with ultra-high strength and good ductility [J]. Mater Sci Eng A, 2012, 539: 42–47.
- [6] LIANG S X, YIN L X, LIU X Y, JING R, ZHOU Y K, MA M Z, LIU R P. Effects of annealing treatments on microstructure and mechanical properties of the Zr345Ti35Al33V alloy [J]. Mater Sci Eng A, 2013, 582: 374–378.
- [7] ZHOU Y K, JING R, MA M Z, LIU R P. Tensile strength of Zr–Ti binary alloy [J]. Chin Phys Lett, 2013, 11: 116201.
- [8] ZHOU Y K, LIANG S X, JING R, JIANG X J, MA M Z, TAN C L, LIU R P. Microstructure and tensile properties of hot-rolled Zr₅₀–Ti₅₀ binary alloy [J]. Mater Sci Eng A, 2015, 621: 259–264.
- [9] XIA C Q, JIANG X J, WANG X Y, ZHOU Y K, FENG Z H, LIANG S X, TAN C L, MA M Z, LIU R P. Microstructure and mechanical properties of hot-rolled ZrB alloys [J]. Mater Sci Eng A, 2015, 628: 168–175.
- [10] FENG Z H, JIANG X J, ZHOU Y K, XIA C Q, LIANG S X, JING R, ZHANG X Y, MA M Z, LIU R P. Influence of beryllium addition on the microstructural evolution and mechanical properties of Zr alloys [J]. Mater Des, 2015, 65: 890–895.
- [11] CHAKRAVARTTY J K, PRASAD Y V R K, ASUNDI M K. Processing map for hot working of alpha-zirconium [J]. Metal Trans A, 1991, 22: 829–836.
- [12] CHAKRAVARTTY J K, BANERJEE S, PRASAD Y V R K, ASUNDI M K. Hot-working characteristics of Zircaloy-2 in the temperature range of 650–950 °C [J]. J Nucl Mater, 1992, 187: 260–271.
- [13] KAPOOR R, CHAKRAVARTTY J K, GUPTA C C, WADEKAR S L. Characterization of superplastic behaviour in the (α + β) phase field of Zr–2.5 wt.% Nb alloy [J]. Mater Sci Eng A, 2005, 392: 191–202.
- [14] KAPOOR R, CHAKRAVARTTY J K. Characterization of hot deformation behaviour of Zr–2.5 Nb in β phase [J]. J Nucl Mater, 2002, 306: 126–133.
- [15] CHAKRAVARTTY J K, KAPOOR R, BANERJEE S, PRASAD Y V R K. Characterization of hot deformation behavior of Zr–1Nb–1Sn alloy [J]. J Nucl Mater, 2007, 362: 75–86.
- [16] SARKAR A, CHAKRAVARTTY J K. Characterization of hot deformation behavior of Zr–1Nb–1Sn alloy [J]. J Nucl Mater, 2013, 440: 136–142.
- [17] LI H, LI M Q, HAN T, LIU H B. The deformation behavior of isothermally compressed Ti-17 titanium alloy in α + β field [J]. Mater Sci Eng A, 2012, 546: 40–45.
- [18] LUO J, LI M Q, LI H, YU W X. Effect of the strain on the deformation behavior of isothermally compressed Ti–6Al–4V alloy [J]. Mater Sci Eng A, 2009, 505: 88–95.
- [19] LI H, LI M Q, ZHANG X Y, LUO J. Characterization of the forgeability of 1Cr11Ni2W2MoV steel using processing map [J]. Mater Sci Eng A, 2010, 527: 6505–6510.
- [20] NING Y Q, FU M W, HOU H Y, YAO Z K, GUO H Z. Hot deformation behavior of Ti–5.0Al–2.40Sn–2.02Zr–3.86Mo–3.91Cr alloy with an initial lamellar microstructure in the α + β phase field [J]. Mater Sci Eng A, 2011, 528: 1812–1818.
- [21] RAO K P, PRASAD Y V R K, HORT N, KAINER K U. Hot workability characteristics of cast and homogenized Mg–3Sn–1Ca alloy [J]. J Mater Process Technol, 2008, 201: 359–363.
- [22] RAO K P, PRASAD Y V R K, DHARMENDRA C, HORT N, KAINER K U. Compressive strength and hot deformation behavior of TX32 magnesium alloy with 0.4% Al and 0.4% Si additions [J]. Mater Sci Eng A, 2011, 528: 6964–6970.
- [23] SESHACHARYULU T, MEDEIROS S C, FRAZIER W G, PRASAD Y V R K. Hot working of commercial Ti–6Al–4V with an equiaxed α - β microstructure: materials modeling considerations [J]. Mater Sci Eng A, 2000, 284: 184–194.
- [24] VIJAYSHANKAR M N, ANKEM S. High temperature tensile deformation behavior of β -Ti alloys [J]. Mater Sci Eng A, 1990, 129: 229–237.
- [25] SRINIVASAN R. Yield points during the high temperature deformation of Ti–15V–3Al–3Cr–3Sn alloy [J]. Scr Metall Mater, 1992, 27: 925–930.
- [26] ANKEM S, SHYUE J G, VIJAYSHANKAR M N, ARSENAULT R J. The effect of volume per cent of phase on the high temperature tensile deformation of two-phase Ti–Mn alloys [J]. Mater Sci Eng A, 1989, 111: 51–61.
- [27] WEISS I, SEMIATIN S L. Thermomechanical processing of beta titanium alloys—An overview [J]. Mater Sci Eng A, 1998, 243: 46–65.
- [28] ZHANG J Q, DI H S, WANG H T, MAO K, MA T J, CAO Y. Hot deformation behavior of Ti-15-3 titanium alloy: A study using processing maps, activation energy map, and Zener–Hollomon parameter map [J]. J Mater Sci, 2012, 47: 4000–4011.
- [29] PHILIPPART I, RACK H J. High temperature dynamic yielding in metastable Ti–6.8Mo–4.5F–1.5Al [J]. Mater Sci Eng A, 1998, 243: 196–200.
- [30] SELLARS C M, TEGART W J. Relation between strength and structure in hot deformation [J]. Mem Sci Rev Met, 1966, 63: 731–746.
- [31] XIA X X, SAKARIS P, MCQUEEN H J. Hot deformation, dynamic recovery, and recrystallisation behaviour of aluminium 6061–SiC_p composite [J]. Mater Sci Technol, 1994, 10: 487–496.
- [32] MEDINA S F, HERNANDEZ C A. General expression of the Zener–Hollomon parameter as a function of the chemical composition of low alloy and microalloyed steels [J]. Acta Metall, 1996, 44: 137–148.
- [33] CHAKRAVARTTY J K, BANERJEE S, PRASAD Y V R K. Superplasticity in β -zirconium: A study using a processing map [J]. Scr Metall Mater, 1992, 26: 75–78.

- [34] LANGDON T G. An analysis of flow mechanisms in high temperature creep and superplasticity [J]. Mater Trans, 2005, 46: 1951–1956.
- [35] SARGENT P M, ASHBY M F. Deformation maps for titanium and zirconium [J]. Scr Metall, 1982, 16: 1415–1422.
- [36] PRASAD Y V R K, SASIDHARA S. Hot working guide: A compendium of processing maps [M]. Materials Park, OH: ASM International, 1997.
- [37] PRASAD Y V R K, SESHACHARYULU T. Modelling of hot deformation for microstructural control [J]. Int Mater Rev, 1998, 43: 243–258.
- [38] ZHOU Ge, DING Hua, CAO Fu-rong, HAN Yin-ben, ZHANG Bei-jiang. Flow instability criteria in processing map of superalloy GH79 [J]. Transactions of Nonferrous Metals Society of China, 2012, 22(7): 1575–1581.
- [39] QIN Chun, YAO Ze-kun, NING Yong-quan, SHI Zhi-feng, GUO Hong-zhen. Hot deformation behavior of TC11/Ti–22Al–25Nb dual-alloy in isothermal compression [J]. Transactions of Nonferrous Metals Society of China, 2015, 25(7): 2195–2205.

温度和应变速率对 $Zr_{50}Ti_{50}$ 合金在 β 单相区热变形行为的影响

周云凯¹, 冯志浩¹, 夏超群¹, 刘文昌¹, 景勤¹, 梁顺星²,
马明臻¹, 张治国¹, 张新宇¹, 刘日平¹

1. 燕山大学 亚稳材料制备技术与科学国家重点实验室, 秦皇岛 066004;
2. 河北工程大学 装备制造学院, 邯郸 056038

摘要: 在温度为 700~850 °C 和应变速率为 0.001~1 s⁻¹ 的条件下, 研究了 $Zr_{50}Ti_{50}$ 合金在 β 单相区的热变形行为和组织演变。流变曲线呈现典型的流变软化特征。在较高的应变速率下, 出现了不连续屈服现象, 这一特点在其他传统锆合金中没有发现。计算得到表观变形激活能为 103 kJ/mol, 并建立了该合金在 β 单相区的流变应力与应变速率和变形温度之间的本构方程。分析表明该合金的热变形机制主要为动态回复, 并且由于较强的动态回复效果而抑制了动态再结晶。随后, 通过计算建立了合金的热加工图, 并根据热加工图找到了合金在 β 单相区的最佳热变形加工参数为温度 830~850 °C, 变形速率为 0.56~1 s⁻¹。

关键词: 锆合金; 热变形; 表观激活能; 显微组织; 加工图

(Edited by Yun-bin HE)